

The Importance of Quantum Pressure of Fuzzy Dark Matter on Lyman-Alpha Forest

Jiajun Zhang^{a,b*}, Jui-Lin Kuo^{c†}, Hantao Liu^{b‡},
Yue-Lin Sming Tsai^{d§}, Kingman Cheung^{c,d,e¶}, and Ming-Chung Chu^{b**}

^a *Department of Astronomy, School of Physics and Astronomy,
Shanghai Jiao Tong University, Shanghai, China,*

^b *Department of Physics, The Chinese University of Hong Kong, Hong Kong, China,*

^c *Department of Physics, National Tsing Hua University, Hsinchu, Taiwan,*

^d *Physics Division, National Center for Theoretical Sciences, Hsinchu, Taiwan, and*

^e *Division of Quantum Phases and Devices, School of Physics,
Konkuk University, Seoul 143-701, Republic of Korea*

(Dated: August 14, 2018)

Abstract

With recent Lyman-alpha forest data from BOSS and XQ-100, some studies suggested that the lower mass limit on the fuzzy dark matter (FDM) particles is lifted up to 10^{-21} eV. However, such a limit was obtained by Λ CDM simulations with the FDM initial condition and the quantum pressure (QP) was not taken into account which could have generated non-trivial effects in large scales structures. We investigate the QP effects in cosmological simulations systematically, and find that the QP leads to further suppression of the matter power spectrum at small scales, as well as the halo mass function in the low mass end. We estimate the suppressing effect of QP in the 1D flux power spectrum of Lyman-alpha forest and compare it with data from BOSS and XQ-100. The rough uncertainties of thermal gas properties in the flux power spectrum model calculation were discussed. We conclude that more systematic studies, especially with QP taken into account, are necessary to constrain FDM particle mass using Lyman-alpha forest.

PACS numbers: 95.35.+d

* liamzhang@sjtu.edu.cn

† juilinkuo@gapp.nthu.edu.tw

‡ htliu@phy.cuhk.edu.hk

§ smingtsai@gate.sinica.edu.tw

¶ cheung@phys.nthu.edu.tw

** mcchu@phy.cuhk.edu.hk

I. INTRODUCTION

Dark matter is one of the intriguing mysteries of modern cosmology. Currently, the leading paradigm of dark matter is the cold dark matter (CDM), supported by the majority of the observations like the mass-to-light ratio of clusters of galaxies [1], the rotation curves of galaxies [2], the Bullet Cluster [3], the cosmic microwave background (CMB) [4] and the large scale structure of the universe [5]. Despite its success on large scales, the CDM paradigm faces three problems on small scales, dubbed as the “small scales crisis” [6]: (i) the missing satellite problem, (ii) the cusp-core problem, and (iii) the too-big-to-fail problem. The essence of these problems is that CDM predicts an excess amount of dark matter on small scales, and hence the key to address them is to smooth out the small-scale structures by astrophysical processes [7], or invoke alternative dark matter models like warm dark matter (WDM) [8], self-interacting dark matter [9] and fuzzy dark matter (FDM) [10].

The FDM paradigm, in which the dark matter is made of ultra-light bosons in Bose-Einstein condensate state, is an ideal alternative of CDM, since it suppresses small-scale structures while inherits the success of CDM on large scales [11–13]. For the detailed history and implementation of FDM, one can see Ref. [14] and the reference therein. The suppression effect, arising from the effective “quantum pressure” (QP) of FDM, is directly connected to the mass of the ultra-light axion. The predictions of FDM with mass $\sim 10^{-22}$ eV are consistent with observations of the CMB and large scales structure [15], high- z galaxies and CMB optical depth [16], and the density profiles of dwarf spheroidal galaxies [17]. However, recent results claimed that FDM with mass below 10^{-21} eV has already been ruled out at 95% confidence level by comparing the results of hydrodynamic simulations to the Lyman-alpha forest data [18–20].

Lyman-alpha forest, a series of absorption lines in the Lyman α emission spectrum from distant galaxies and quasars by neutral hydrogen (HI) gas at different redshift, provides the information about the the spatial distribution of HI gas at high redshift. In the leading theory of Lyman-alpha forest — the gravitational confinement model — HI clumps are confined by the gravity provided by dark matter halos [21, 22]. Thus, the flux power spectrum of Lyman-alpha forest is a biased representation of the underling DM density field power spectrum [23–25]. Recently, two collaborations, the Baryon Oscillation Spectroscopic Survey (BOSS) [26] and XQ-100 [27], have announced their analyses between redshift $z = 2 - 5$ for the flux power spectrum, thus providing tools to constraint dark matter models on an unprecedented high level of precision.

To robustly exclude such a mass range, two tasks have to be carried out before the experimental data analysis. The first is numerical simulations of the FDM system on large scales, which have been performed in a number of approaches: directly solving the Schrödinger-Poisson system [17], Smoothed Particle Hydrodynamic (SPH) simulation [28], and N-body simulation with Particle-Mesh (PM) method [29]. However, all these simulations were restricted in simulation scale and suffered from the singularity problem at zero-density points in the calculation of QP. In this paper, we adopt an independent simulation scheme developed in Ref. [30], which provides DM-only simulations with SPH and particle-particle

(PP) interactions to account for QP, is feasible for implementation in cosmological scale simulations, and avoids the singularity problem.

The second is the uncertainties in hydrodynamic simulations. In the N-body simulation, the uncertainty in the matter power spectrum is $\mathcal{O}(10\%)$ originating from the use of different initial conditions, the adoption of different orders of Lagrangian perturbation theory [31], finite-box effect [32] and the usage of different N-body simulation codes [33–35]. These uncertainties can be precisely estimated and controlled because their properties are well studied. In contrast, the uncertainties from hydrodynamic simulations can be of orders of magnitude [34–37]. Different treatments introduced in hydrodynamic simulations in handling the gaseous part induce huge discrepancy in gas density, gas temperature and galaxy structure. Moreover, different hydrodynamic simulation codes contribute uncertainties to the 1D flux power spectrum at the level of 5%. As stated in Ref. [38], several additional astrophysical processes may also alter the 1D flux power spectrum, such as patchy reionization and smoothing.

We estimate the constraint on the mass range of FDM from Lyman-alpha forest data with DM-only cosmological simulations in four different settings: (1) standard CDM simulation, (2) simulation using FDM-modified initial condition and CDM dynamics, (3) simulation using FDM-modified initial condition and dynamics with FDM mass equals to 2.5×10^{-22} eV, (4) 2.5×10^{-23} eV. By utilizing the 1D flux power spectrum of the CDM hydrodynamic simulation in Ref. [18], one can obtain the 1D flux power spectrum for the corresponding condition using the 3D power spectrum ratio from our simulations.

Our results are shown in the aspects of density field, halo mass function, 3D power spectrum and 1D flux power spectrum with Lyman-alpha forest data. We show that the effect of QP in structure formation is non-trivial and introduce important suppression in the growth of structures. Inspired by the linear theory summarized in Ref. [39], we have calculated the uncertainty range of the 1D flux power spectrum based on the unknown hydrogen gas temperature properties. The suppression of the 1D flux power spectrum from higher gas temperature behaves like the suppression caused by FDM.

This paper is arranged as follows. In Sec. II, we discuss the methodology of the simulation, simulation set-up and initial conditions. We also review the linear theory of 1D flux power spectrum calculation. In Sec. III, we present our results in the aspects of density field, halo mass function, 3D power spectrum and 1D flux power spectrum. We compare our 1D flux power spectrum to the Lyman-alpha forest data. In Sec. IV, we discuss the gas temperature uncertainty. Finally, we summarize our outcomes in Sec. V.

II. METHODOLOGY

A. Quantum Pressure as particle-particle interaction

Standard N-body simulations have problems in calculating the QP because of the discretization of the density field by the delta function. From the expression of QP, obviously,

what we need in the calculation is a smooth density field. There are already some reliable smoothing particle methods used in the N-body simulation of the FDM system with limited box sizes ($< 10h^{-1}$ Mpc), e.g., Ref. [28, 29]. For the sake of Lyman α forest, it is important to have a cosmological scale simulation so that the study of structure formation and matter power spectrum on large scales is possible.

We proposed a novel N-body simulation scheme for FDM in a previous work [30], in which the delta function is replaced by a smooth Gaussian kernel function to solve the singularity problem and avoid the simulation crash. This scheme can be used to perform simulations at scales no smaller than $50h^{-1}$ Mpc as we shall prove later and give a coarse-grained description on small scales. However, the original scheme requires some modifications for cosmological simulations. In this section, we will demonstrate how to embed QP in the cosmological simulations.

For cosmological simulations, one has to consider the transformation from physical to comoving coordinates. Under the transformation described in Appendix A, there is an additional pre-factor a^{-2} for the original QP defined in Ref. [30], where a is the cosmological scale factor. The QP for a cosmological simulation becomes

$$Q = -\frac{\hbar^2}{2m_\chi^2 a^2} \frac{\nabla^2 \sqrt{\rho}}{\sqrt{\rho}}, \quad (1)$$

, where \hbar , m_χ , and ρ are the reduced Planck constant, FDM particle mass and the mass density of FDM, respectively. The corresponding acceleration can be written as

$$\ddot{\mathbf{r}} = \frac{4M\hbar^2}{M_0 m_\chi^2 \lambda^4 a^2} \sum_j \mathcal{B}_j \exp\left[-\frac{2|\mathbf{r} - \mathbf{r}_j|^2}{\lambda^2}\right] \left(1 - \frac{2|\mathbf{r} - \mathbf{r}_j|^2}{\lambda^2}\right) (\mathbf{r}_j - \mathbf{r}), \quad (2)$$

where M , M_0 , λ , and \mathcal{B}_j are the mass of the simulation particle, a normalization factor accounting for the volume ΔV_j occupied by simulation particles, the de Broglie wavelength of FDM particles, and the correction factor for high-density regions, respectively. For more detailed explanations of \mathcal{B}_j , please refer to Appendix A of Ref. [30].

To demonstrate the effect of QP, we consider a two-particle system separated by a distance of order $\mathcal{O}(\text{kpc})$, and the acceleration caused by QP will be $\mathcal{O}(\hbar^2 m_\chi^{-2} \lambda^{-3}) \sim \mathcal{O}(10^{-10} \text{ m s}^{-2})$. In Fig. 1, the QP effect is presented in the plane of (r, \ddot{r}) . The acceleration from QP, gravity, and their sum are shown by the black dashed line, blue solid line, and red solid line, respectively. Apparently, the effect of QP is attractive if the separation between the two particles is shorter than $\lambda/\sqrt{2}$, otherwise repulsive. To understand this phenomenon, we refer back to the definition of QP in Eq. (1): Q is proportional to the curvature of the density, which can be negative, positive, or zero, physically corresponding to negative, positive, and zero forces, respectively. The reason of the difference between Fig. 1 here and the Fig. 1 of [30] is that the mass of the simulation particle is changed from $10^6 M_\odot$ to $\sim 10^8 M_\odot$. The effect of gravity is directly related to the mass of the simulation particles while the QP is not affected due to the fact that the normalization factor M_0 in Eq. (2) is chosen to be the same as the mass of the simulation particles. In other words, the strength of QP is a quantity independent of the simulation particle mass M . Therefore,

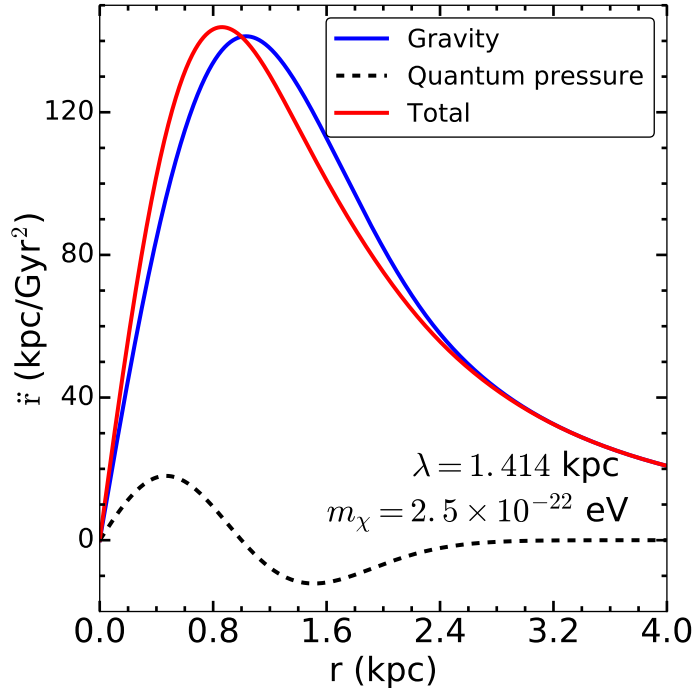


FIG. 1: The acceleration from QP (black dashed line), gravity (blue solid line), and their sum (red solid line) vs. the distance between two particles. Notice that QP is at least 1 order of magnitude smaller than the gravity in the simulation.

the acceleration of gravity is considerably larger in a cosmological simulation due to the larger mass of the simulation particles. Thus, the structure formation in large scales is still dominated by gravity. However, the QP plays a non-trivial role in the structure formation, particularly in highly non-linear regions such as dark matter halos.

B. Simulation settings

We use the code `Gadget2` [40], which is a `TreePM` hybrid N-body code, to perform our simulations. To describe QP, we discretize the interaction term and modify `Gadget2`¹ to calculate QP in the same way as in Ref. [30]. (The PM method is helpful for cosmological simulations with periodic boundary conditions.) Because QP behaves like a short-range force, we adopt the original PM code to compute the long-range force and modify the `Tree` code which takes care of the short-range force to include the calculation of QP. In addition, it is not necessary to set softening length for QP since QP is finite in the $(\mathbf{r}_j - \mathbf{r}) \simeq 0$ region.

We start our simulation from the redshift $z = 99$. The related cosmological parameters are DM energy density $\Omega_m = 0.3$, cosmological constant $\Omega_\Lambda = 0.7$, baryon energy density

¹ The code is called `Axion-Gadget`, publicly available at <https://github.com/liambx/Axion-Gadget>

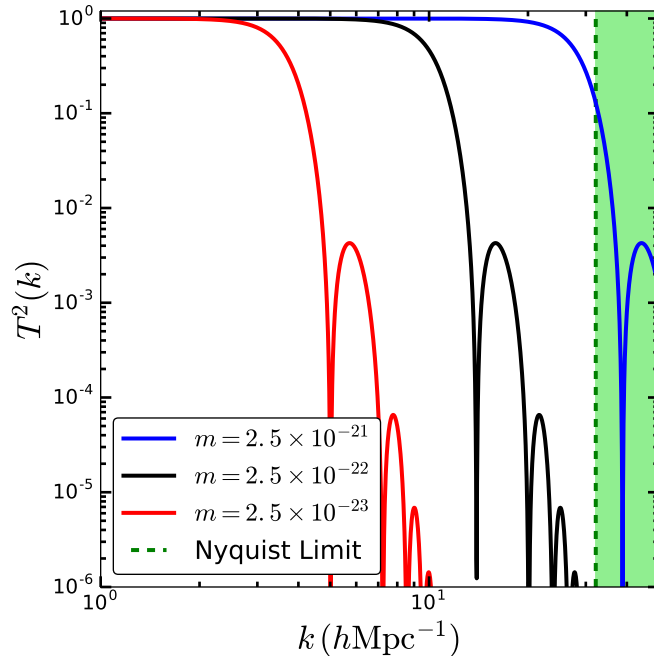


FIG. 2: Initial condition transfer function squared vs. the wavenumber. The blue, black, and red solid lines correspond to FDM masses of 2.5×10^{-21} eV, 2.5×10^{-22} eV, 2.5×10^{-23} eV, respectively. The green dashed line is the Nyquist Limit which is the resolution limit of our simulation, and so the light green region is not trustworthy. The suppression of the power spectrum in small scales depends on the mass of the FDM particles [41]: the smaller the FDM particle mass, the larger the suppression scale will be.

$\Omega_b = 0.04$, dimensionless Hubble parameter $h = 0.7$, scalar spectral index $n_s = 0.96$, and the power spectrum normalization factor $\sigma_8 = 0.8$.

We generated the initial CDM power spectrum following Ref. [42]. The suppression of the FDM power spectrum relative to the CDM one on small scales can be characterized by a transfer function $\mathcal{T}(k, z)$ [41]

$$P_F(k, z) = \left[\frac{\mathcal{T}_{\text{FDM}}(k, z)}{\mathcal{T}_{\text{CDM}}(k, z)} \right]^2 P_C(k, z) = \mathcal{T}^2(k, z) P_C(k, z), \quad (3)$$

where k is the wavenumber and $P_F(k, z)$ and $P_C(k, z)$ are the three-dimensional power spectra of FDM and CDM, respectively. One has to bear in mind that the physical difference between $\mathcal{T}_{\text{CDM}}(k, z)$ and $\mathcal{T}_{\text{FDM}}(k, z)$ ² is characterized by the transfer function $\mathcal{T}(k, z)$, which

² The transfer functions $\mathcal{T}_{\text{FDM}}(k)$ and $\mathcal{T}_{\text{CDM}}(k)$ are defined in Eq. (1) of Ref. [42], which transfer the power spectrum at large scales ($k = 0$) to the power spectrum at other scales ($k \neq 0$) for the corresponding model. Restricted to linear theory, the current matter power spectrum $P(k)$ would be proportional to the product of the primordial power spectrum $P_{\text{prim}}(k)$ given by inflation theory and $\mathcal{T}^2(k)$ embodying the

transforms the power spectrum from CDM to FDM and so is deduced as the ratio of FDM transfer function $\mathcal{T}_{\text{FDM}}(k, z)$ to CDM transfer function $\mathcal{T}_{\text{CDM}}(k, z)$.

Following the arguments in Ref. [43], we can well approximate $\mathcal{T}(k, z)$ by the redshift-independent expression [10]

$$\mathcal{T}(k) = \frac{\cos x^3}{1 + x^8}, \quad \text{where } x = 1.61 \times \left(\frac{m_\chi}{10^{-22} \text{ eV}} \right)^{1/18} \times \frac{k}{k_J}, \quad (4)$$

The parameter $k_J = 9(m_\chi/10^{-22} \text{ eV})^{1/2} \text{Mpc}^{-1}$ is the critical scale of Jeans wavenumber at matter-radiation equality. In Fig. 2, we present the square of the transfer function $\mathcal{T}^2(k)$ with three different FDM masses to demonstrate the suppression of FDM power spectrum in small scales relative to CDM power spectrum. The blue, black, and red solid lines correspond to the masses of the FDM being $2.5 \times 10^{-21} \text{ eV}$, $2.5 \times 10^{-22} \text{ eV}$, $2.5 \times 10^{-23} \text{ eV}$, respectively. The vertical green dashed line represents the Nyquist limit which is the resolution limit of our simulations and the corresponding wavenumber k_{Ny} is computed to be

$$k_{Ny} = \pi \left(\frac{N_0}{V_0} \right)^{1/3},$$

where V_0 is the volume of the simulation box, and N_0 is the total number of simulation particles, which are $(50h^{-1} \text{Mpc})^3$ and 512^3 respectively in our simulations. The origin of this limit is due to the fact that each simulation particle has an approximate average volume $(V_0/N_0)^{1/3}$ and we cannot know what happens inside the simulation particle. In other words, the result is not reliable for $k > k_{Ny}$. One can see that there is a sharp break of FDM power spectrum at $k \sim k_J$ and severe oscillations occur with suppression for $k > k_J$ for all three different FDM masses. For a smaller mass, the suppression is tremendous compared to a larger mass which behaves almost the same as the CDM case at high k .

We modify the code 2LPTic [44] for generating the initial conditions of the CDM power spectrum for cosmological simulations to incorporate the transfer function so as to generate initial conditions with the FDM power spectrum.

C. 1D Flux Power Spectrum

The calculation of the 1D flux power spectrum in the linear regime is well summarized in Ref. [39],

$$P_b = \frac{P_{DM}}{(1 + k^2/k_J^2)^2}, \quad (5)$$

$$P_F(k_z, z) = \int_{k_z}^{\infty} \frac{k dk}{2\pi} P_b(k, z) W(k, k_z). \quad (6)$$

growth of structure, $P(k) \propto \mathcal{T}^2(k) P_{\text{prim}}(k)$. At the super-horizon scale, cosmological perturbation theory shows that the structure does not grow, and hence the transfer function is set with boundary condition $\mathcal{T}(0) = 1$.

First, the linear dark matter power spectrum P_{DM} was calculated by CAMB [45], with the same parameters used in the simulations. Then we calculate the baryon power spectrum from Eq. (5), in which k_J is the Jeans wavenumber related to the Jeans length λ_J by

$$k_J = \frac{2\pi}{\lambda_J}. \quad (7)$$

Finally, we integrate Eq. (6) to get the one-dimensional flux power spectrum, in which we need the bias function

$$W = A \exp\left(-\frac{k_z^2 b_0^2}{2H^2}\right) \left[1 + \frac{\Omega_m^{0.6}}{2 + 0.7(1 - \gamma)} \frac{k_z^2}{k^2} - \frac{\gamma - 1}{4[2 + 0.7(1 - \gamma)]} \frac{k_z^2 b_0^2}{H^2}\right]^2. \quad (8)$$

Here

$$b_0(z) = \sqrt{\frac{2k_B T_0(z)}{m_H}}$$

is a parameter related to the velocity dispersion of the HI gas at redshift z , and $T_0(z)$ is the average temperature of HI gas at redshift z . $\gamma(z)$ is the polytropic index in the equation of state of HI gas³. A is a normalizing factor, whose effect is the same as the parameter σ_8 in P_{DM} .

For further calculation, we use a power-law parametrization of $T(z)$ and $\gamma(z)$

$$T_0(z) = T_0^A \left[\frac{1+z}{5.5}\right]^{T_0^S}, \quad \gamma(z) = \gamma^A \left[\frac{1+z}{5.5}\right]^{\gamma^S}, \quad (9)$$

where the 1σ uncertainty ranges are

$$T_0^A = 9.2_{-0.1}^{+1.2} 10^3 \text{ K}, \quad T_0^S = -2.5_{-0.5}^{+0.45}, \quad \gamma^A = 1.64_{-0.26}^{+0.01}, \quad \gamma^S = -0.15_{-0.61}^{+1.25}. \quad (10)$$

These are copied from the Table. II in Ref. [46]. As for σ_8 and λ_J , we treat them as redshift independent constants with the 1σ uncertainty ranges as in Ref. [4, 47]

$$\sigma_8 \in [0.78, 0.88], \quad \lambda_J = 100 \pm 80 \text{ kpc}. \quad (11)$$

The formulae discussed above are only applicable to linear perturbation, and the insertion of non-linear matter power spectrum in Eq. (6) is problematic. However, for the sake of simplicity, the 1D flux power spectrum is assumed to be related to the DM density power spectrum with the following equation,

$$P_F(k_z, z) = \int_{k_z}^{\infty} \frac{k dk}{2\pi} P_{DM}(k, z) W(k), \quad (12)$$

³ For an ideal polytropic gas, the temperature at redshift z and position \mathbf{x} is

$$T(z, \mathbf{x}) = T_0(z) (1 + \delta_b(\mathbf{x}))^{\gamma(z)-1}.$$

which is inspired by the linear theory. Here W represents the bias introduced by the thermal properties of intergalactic medium (IGM), but the distortions in the direction of line-of-sight is neglected. Given the form of Eq. (12), the 1D flux power spectrum is the 3D matter power spectrum convolved with the bias W along the line of sight. On one hand, we assume that the dynamics of dark matter does not affect the gaseous component, and the bias W is the same in all four different simulations. On the other hand, we reweigh the matter power spectrum P_{DM} with the 3D matter power spectrum ratio of the simulations **FDM/FIC/F23** to the simulation **CDM**. That is to say, we first take the derivative of the 1D flux power spectrum P_F , from the mock 1D flux power spectrum in hydrodynamic simulation shown in Ref. [48], with respect to k_z

$$-\frac{2\pi}{k_z} \frac{dP_F}{dk_z} = P_{DM}W, \quad (13)$$

and multiply the right hand side (RHS) of this equation by the ratio P_i/P_{CDM} , where $i = \mathbf{FDM}, \mathbf{FIC}$ and **F23**. Then we integrate this expression to get the modified 1D flux power spectrum

$$P_{F,i}(k_z, z) = \int_{k_z}^{\infty} \frac{kdk}{2\pi} \frac{P_i(k, z)}{P_{CDM}(k, z)} P_{DM}(k, z) W(k). \quad (14)$$

By comparing the modified $P_{F,i}$ and the original P_F , we can tell the effect of FDM model on Lyman alpha forest.

III. NUMERICAL RESULT

Abbreviations	Initial Conditions	Dynamics	FDM mass m_χ
CDM	CDM-Standard	CDM-Standard	—
FIC	FDM-modified	CDM-Standard	2.5×10^{-22} eV
FDM	FDM-modified	FDM-modified	2.5×10^{-22} eV
F23	FDM-modified	FDM-modified	2.5×10^{-23} eV

TABLE I: The abbreviations and details of simulations we have performed.

We have performed four different kinds of simulations for comparison as listed in Table. I. To avoid words cluttering in the following presentation, we use abbreviations for these four simulations. In this section, we first present the density field of the simulation **FDM** as well as the density field difference between the simulations **FDM** and **FIC**. We then compare the 3D power spectra and 1D flux power spectra of all four simulations in order to investigate the non-linear effect of the QP. After showing the 1D flux power spectrum, a numerical chi-square test of Lyman-alpha forest data from BOSS and XQ-100 is performed. Finally, we discuss the constraint on the FDM mass.

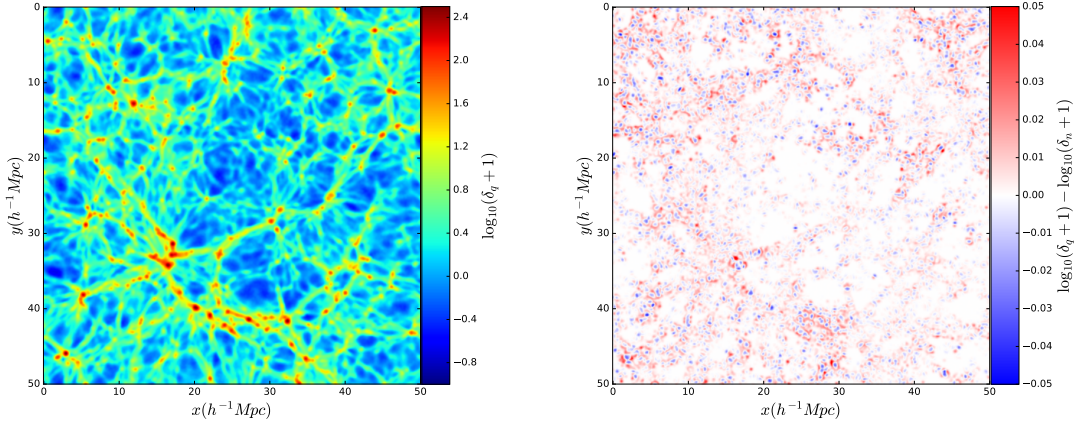


FIG. 3: Left panel: the density field of the simulation **FDM**. This figure is a slice from the simulation cube. The color scale represents the log scale of density contrast δ_q . Right panel: the difference of density field between the simulation **FDM** and the simulation **FIC**. The color scale represents the log scale of the density difference between the mentioned two simulations. δ_n is the density contrast of the simulation **FIC**.

A. Density Field and Halo Mass Function

In the left panel of Fig. 3, we depict the density field taken from a slice of the simulation cube. The slice is $0.5 h^{-1} \text{Mpc}$ thick, and the density field is calculated from the particle distribution by the triangular shaped cloud (TSC) scheme but further smoothed by a Gaussian filter (variance $\sigma = 0.15 h^{-1} \text{Mpc}$) for better illustration. With the color scale, one can clearly see that the large scales structures include voids, filaments and knots. The density contrast δ_q is defined as

$$\delta_q = \frac{\rho_q}{\bar{\rho}_q} - 1,$$

where the subscript q denotes that it is from the simulation **FDM**. The color scale of Fig. 3 represents the logarithm of $\delta_q + 1$, which is the ratio of local density ρ_q to the average density $\bar{\rho}_q$. In the right panel of Fig. 3, we compare the density field of the simulation **FDM** and the simulation **FIC**. The color scale shows the difference between the logarithm of $\rho_q/\bar{\rho}_q$ and the logarithm of $\rho_n/\bar{\rho}_n$.

We found that the difference between the density fields of the two simulations **FDM** and **FIC** is small, but the effect of QP can produce granular structures close to the high density regions. Note that these granular structures are indeed due to QP, but not the difference in the initial conditions by comparing the density fields of the simulations **FIC** and **CDM**.

To illustrate more details in small scale, we select a $5h^{-1}\text{Mpc}$ sub-box projected in y direction and zoom in for better resolution. In Fig. 4, the left panel is from the simulation **FDM** and the right panel is from the simulation **FIC**. The density field is calculated from the particle distribution by the nearest grid point scheme and further smoothed by bilinear

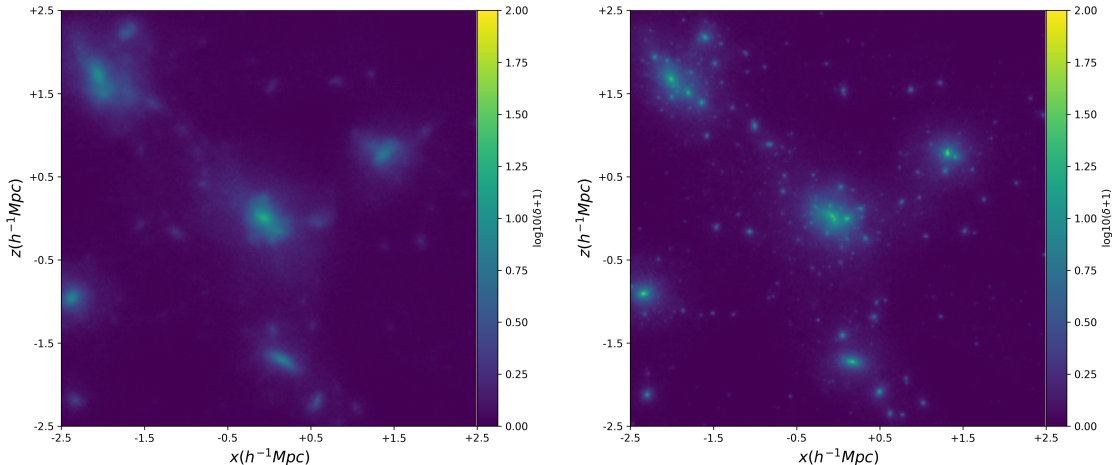


FIG. 4: A $5h^{-1}\text{Mpc}$ sub-box density field projected in y direction from the simulation **FDM** (on the left) and the simulation **FIC** (on the right). The color scale represents the log scale of density. The substructure on the left panel (**FDM**) is suppressed under the influence of QP.

algorithm. We note that the cluster in the simulation **FDM** looks much fuzzier than the one in the simulation **FIC**. Qualitatively, the formation of low mass halos is further suppressed when taking QP into consideration.

We identified the halos using the package **AHF** [49], which can build up the hierarchical structure for the halos and sub-halos in the snapshots of our simulations. The halos are identified if the average density of the halo is over 200 times the critical density of the universe. In Fig. 5, the halo mass function is presented with the FDM mass $m_\chi = 2.5 \times 10^{-22} \text{eV}$. The colors represent different redshifts, and the solid, dot-dashed and dashed lines represent the halo mass function of the simulations **CDM**, **FIC** and **FDM**, respectively. The break of the halo mass functions at $M = 2.3 \times 10^9 h^{-1} M_\odot$ (the green dashed line) is due to our limited resolution. By definition, we cannot identify halos whose mass is below $2.3 \times 10^9 h^{-1} M_\odot$. From halo masses $5 \times 10^{11} h^{-1} M_\odot$ to $2 \times 10^{13} h^{-1} M_\odot$, there is no recognizable difference among the simulations **FDM**, **FIC** and **CDM**. However, for halo mass below $5 \times 10^{11} h^{-1} M_\odot$, the difference becomes noticeable.

To quantitatively see the difference, one can refer to the right panel of Fig. 5 which manifestly demonstrates the suppression caused by the QP and the modified initial condition. We can see that QP (**FDM** simulation) introduces 20% more suppression on the number density of $M < 2 \times 10^{11} h^{-1} M_\odot$ halos than that of **FIC** simulation, with modified initial condition only. There is no identifiable effect in the simulations **FDM** and **FIC** for the halo mass function with $M > 5 \times 10^{11} h^{-1} M_\odot$.

It is clear that the difference in modified initial conditions and QP start to have significant influence on the formation of halos. Furthermore, it is worth mentioning that by using the code established in Ref. [30] we are able to explore halo mass smaller than

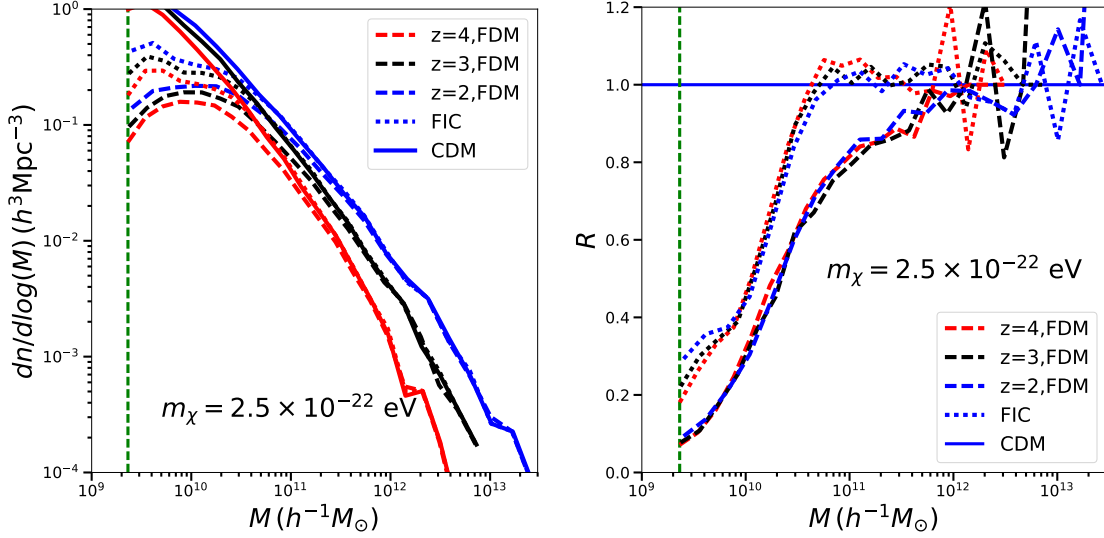


FIG. 5: Left panel: The halo mass function measured from the simulation **FDM** (dashed line), **CDM** (solid line) and **FIC** (dotted line) for redshift $z = 4, 3, 2$ (red, black, blue). Right panel: The respective halo mass function ratios between the simulation **FDM** (dashed line), **FIC** (dotted line) and **CDM** for redshift $z = 4, 3, 2$ (red, black, blue). Here the FDM mass is $m_\chi = 2.5 \times 10^{-22}$ eV. The abscissa axis is the mass of the halo and the ordinate axis is the number density per halo mass in log scale. The number density of low mass halos is further suppressed under the influence of QP by $\sim 20\%$, if we compare the halo mass function ratio of **FDM** with that of **FIC**.

$2 \times 10^{13} h^{-1} M_\odot$ in cosmological simulations.

B. Impacts on Lyman-Alpha Forest

Here we investigate the difference in the 1D flux power spectrum among our four simulations with the method mentioned in Sec.II C, which enables us to quantitatively study the effect of the modified initial condition and dynamics introduced by FDM. Furthermore, our result of 1D flux power spectrum will be used to compare with the BOSS/XQ-100 data.

In Fig. 6, we compare the 3D power spectra at different redshifts among different simulations **CDM**, **FIC**, **FDM** and **F23**. In the left panel of Fig. 6, the effect of FDM initial condition is almost negligible at low redshifts but plays an important role at high redshifts. However, the effect of QP is non-negligible even at low redshifts. During the non-linear gravitational evolution even without the QP, the power spectrum of the simulation **FIC** grows differently from the simulation **CDM**. However, at $z = 0$ the power spectra of the simulations **FIC** and **CDM** almost overlap, and one can barely see the difference between them. The effect of the FDM initial condition turns out to be a tiny suppression on power spectrum at low redshifts.

On the other hand, the power spectrum of the simulation **FDM** is clearly different from the simulations **FIC** and **CDM** at low redshifts because of the non-trivial QP effect.

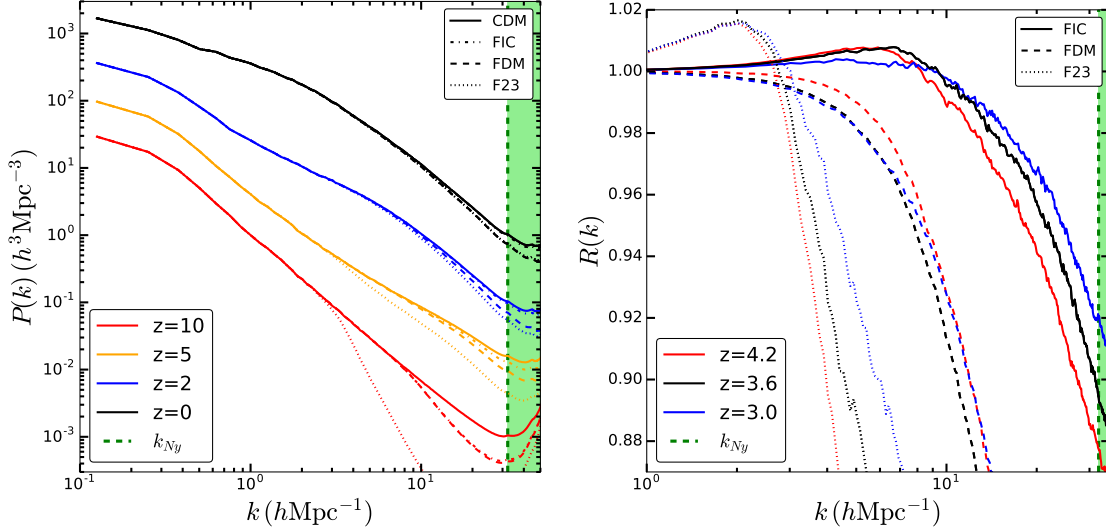


FIG. 6: Left panel: the 3D power spectrum measured from the simulations **CDM** (in solid lines), **FIC** (in dot-dashed lines), **FDM** (in dashed lines) and an additional simulation **F23** with $m_\chi = 2.5 \times 10^{-23}$ eV (in dotted lines). Right panel: the relative non-linear matter power spectrum measured from the simulation. The ordinate axis $R(k)$ is the ratio of the 3D power spectra of the simulations **FDM** (in dashed lines), **FIC** (in solid lines) and **F23** (in dotted line) to that of the simulation **CDM**. Different colors represent different redshifts. The green dashed line represents the corresponding wavenumber of the Nyquist limit.

For the power spectrum of the simulation **F23**, the suppression on small scales is even more significant than all other simulations due to its larger QP.

In the right panel of Fig. 6, we show the ratio $R(k)$ of the 3D power spectra from the simulations **FDM**, **FIC** and **F23** to that of simulation **CDM**. One can see that the QP suppresses the power spectrum by 2 – 5% relative to the simulation **FIC** at $k < 10 h \text{ Mpc}^{-1}$ for three different redshifts $z = 3.0, 3.6, 4.2$. However, for $k < 1 h \text{ Mpc}^{-1}$, the 3D power spectra from the simulations **FDM**, **FIC** and **F23** are identical. Therefore, we can conclude that, QP has no effect on large scale, which is well-expected. For $k > 10 h \text{ Mpc}^{-1}$, since it is approaching our resolution limit, the results should be taken carefully and critically. The effect of QP in the simulation **F23** is clearly more significant than the simulation **FDM**.

The 1D flux power spectra are shown in the left panel of Fig. 7 for comparison with the data of BOSS and XQ-100 at three different redshifts $z = 3.0, 3.6, 4.2$. The solid, dot-dashed, dashed and dotted lines represent 1D flux power spectra from the simulations **CDM**, **FIC**, **FDM** and **F23**, respectively. The dots and error bars are the data from BOSS in darker colors and XQ-100 in lighter colors. At the small-scale region $10^{-2} \text{ km}^{-1} \text{ s} < k < 10^{-1} \text{ km}^{-1} \text{ s}$, which corresponds to $1 h \text{ Mpc}^{-1} < k < 10 h \text{ Mpc}^{-1}$ in the discussion of the matter power spectrum, the 1D flux power spectra for the simulations **FDM** and **F23** are relatively more suppressed than those of **CDM** and **FIC**. Although the simulation **FIC** differs from **CDM** in the initial condition, the difference in their spectra is still small.

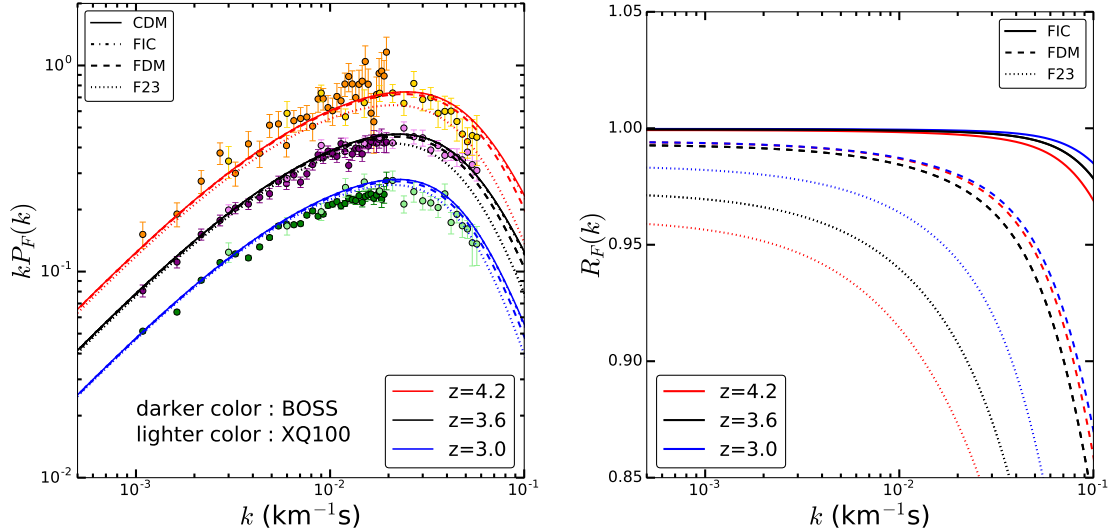


FIG. 7: Left panel: the 1D flux power spectra from the simulations **CDM** (in solid lines), **FIC** (in dot-dashed lines), **FDM** (in dashed lines) and **F23** (in dotted lines), with the data from BOSS (darker color) and XQ-100 (lighter color) at different redshifts (different color). The ordinate axis is the wavenumber k times the 1D flux power spectrum and the abscissa axis is the corresponding wavenumber. Right panel: the impact of non-linear effect on the 1D flux power spectrum. The ordinate axis is the ratio of 1D flux power spectra of the simulations **FDM** (in dashed lines), **FIC** (in solid lines) and **F23** (in dotted line) to that of the simulation **CDM** and the abscissa axis is the corresponding wavenumber. The colors represent different redshifts.

The right panel of Fig. 7 shows the ratio $R_F(k)$ of the 1D flux power spectra of the simulations **FIC**, **FDM** and **F23** to that of the simulation **CDM**. The degree of suppression is up to 10% at $k \simeq 10^{-1} \text{ km}^{-1} \text{ s}$ for the simulation **FDM**. Additionally, the 1D flux power spectrum of the simulation **F23** is suppressed even more than the simulation **FDM**. On the contrary, the degree of suppression is smaller than 4% at $k \simeq 10^{-1} \text{ km}^{-1} \text{ s}$ for the simulation **FIC**. For $k < 10^{-2} \text{ km}^{-1} \text{ s}$, the difference in the 1D flux power spectra for the simulations **FDM**, **FIC** and **CDM** is less than 2%. In fact, the QP contribution cannot be neglected even if the QP is sub-dominant as shown in Fig. 1.

Finally, it is clear that a full investigation of hydrodynamic simulations with the QP is necessary to robustly constrain the mass region of FDM.

IV. DISCUSSION

It has been reported in Ref. [18–20] that the FDM mass can be excluded up to 10^{-21} eV at 2σ significance. However, the systematic uncertainties arising from both simulation (N-body and hydrodynamics) and gas properties (like the temperature of gas) were not discussed adequately in these works.

m_χ	$\Delta T_{0,\max}$
2.5×10^{-22} eV	1.5×10^3 K
5×10^{-22} eV	2×10^2 K
10^{-21} eV	1×10^2 K

TABLE II: For each FDM mass m_χ , the gas temperature uncertainty should be less than $\Delta T_{0,\max}$ for any confirmation or exclusion to be valid.

Note that the well-known discrepancies in simulation will introduce uncertainties on the observables, e.g. the code-to-code inconsistency in hydrodynamic simulations introduces at least $\sim 5\%$ uncertainty in 1D flux power spectrum as shown in Ref. [50, 51]. A brief discussion of the uncertainties in simulation is given in Appendix B for interested readers.

In the previous section, we consider the effects of FDM. However, the thermal properties of IGM also impact the 1D flux power spectrum, as shown in Eq. (6) and Eq. (12). Since these two effects are degenerate in the linear power spectrum, one should consider them simultaneously before reaching any conclusion. In this subsection, we will discuss the possible uncertainty caused by the gas temperature and compare it with that cause by FDM mass to see their degeneracy in the power spectrum.

First, as an illustration of the potential effects of gas, we consider the prediction of the linear theory and its uncertainty. There are several parameters in Eq. (6), but for simplicity we only consider the uncertainty of FDM particle mass m_χ and average gas temperature T_0 . The error of the 1D flux power spectrum can be expressed as

$$\frac{\Delta P_F}{P_F} = \frac{\partial \ln P_F}{\partial m_\chi} \Delta m_\chi + \frac{\partial \ln P_F}{\partial T_0} \Delta T_0. \quad (15)$$

We apply this formula to the linear 1D power spectrum at redshift $z = 3.0$ and set $\gamma = 1.64(1 + 3/5.5)^{-0.15} = 1.72$, $\lambda_J = 100$ kpc in the calculation of partial derivatives. For the most optimistic estimation, we set $\Delta P_F = 0$, so that we can express Δm_χ in terms of ΔT_0 . In a most conservative precision $\Delta m_\chi/m_\chi < 100\%$, one can obtain a maximum temperature uncertainty $\Delta T_{0,\max}$ and compare it to the current uncertainty of T_0 . From Eq. (10), the best-fit and 1σ uncertainty of T_0 at redshift $z = 3$ is about

$$T_0 = 20_{-3}^{+7} \times 10^3 \text{ K}.$$

For FDM mass $m_\chi = 2.5 \times 10^{-23}$ eV, $\Delta T_{0,\max}$ is larger than 10^4 K. Therefore we can actually exclude this kind of FDM model robustly with Lyman-alpha observation. However, for FDM mass in the range from 10^{-22} eV to 10^{-21} eV, we need much higher precision of the temperature to draw the conclusion (see Table. II).

Second, we use a similar method as in Sec. IIIB, with one difference in the RHS of Eq. (13); we multiply the ratio of bias function W with different gas temperature rather than the ratio of matter power spectra,

$$P_{F,\text{thermal}}(k_z, z) = \int_{k_z}^{\infty} \frac{k dk}{2\pi} P_{DM}(k, z) W(k) \frac{W(k_z, k, T_0)}{W(k_z, k, T_{0,\text{bestfit}})}. \quad (16)$$

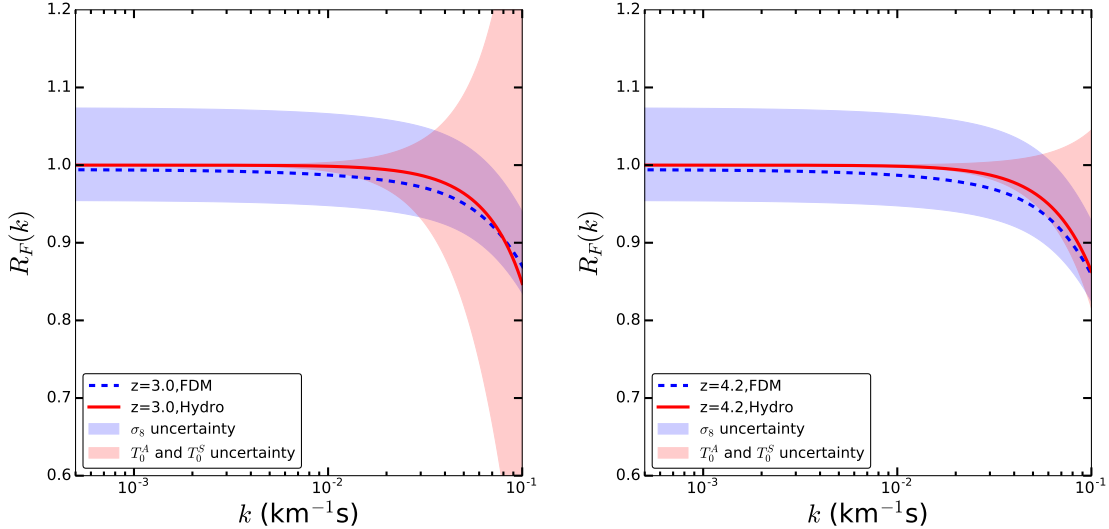


FIG. 8: Left (right) panel: the ratios of 1D flux power spectrum at $z = 3.0$ ($z = 4.2$). The blue dashed lines show the effect of FDM whose $m_\chi = 2.5 \times 10^{-22}$ eV measured from the simulations. The blue shaded area shows the 1σ uncertainty range of σ_8 transferred to the normalization factor of the matter power spectrum. The red lines illustrate the effect of changing the temperature of the gas, which look similar to the blue dashed lines as an example. The red shaded area shows the 1σ uncertainty range of T_A and T_S . We can see that the suppression caused by FDM is fully contained within the uncertainty range of temperature, and so it is difficult to tell whether the suppression is due to dynamics or different temperatures of the gas.

Here we used the Bias function in the linear theory Eq. (8). Even though at the redshift range $z = 3$ to 4 , the structure in the universe is non-linear, we still use the ratio predicted by linear theory because our purpose here is to demonstrate the uncertainty of gas temperature instead of studying the thermal properties of gas which requires full hydrodynamics simulation.

As in Sec. III B, we will calculate the ratio $R_F = P_{F,thermal}/P_F$ again and compare it with the suppression induced by FDM. The best-fit value $T_{0,bestfit}(z)$ is calculated from Eq. (9) with $T_{0,bestfit}^A = 9.2 \times 10^3$ K and $T_{0,bestfit}^S = -2.5$. The upper limit in the red shaded region in Fig. 8 is given by $T_0^A = 9.1 \times 10^3$ K and $T_0^S = -2.05$ while the lower limit corresponds to $T_0^A = 10.4 \times 10^3$ K and $T_0^S = -3$, which are chosen according to the 1σ uncertainty Eq. (10). From Fig. 8, it is obvious that the current constraint on the temperature of gas is not good enough to exclude FDM mass $m_\chi = 2.5 \times 10^{-22}$ eV, let alone the fact that we have not even included the uncertainties of other thermal parameters of the gas. A detailed study of the thermal properties of the gas is needed to settle the issue.

Finally, as Hui et al. pointed out in Ref. [38], several additional astrophysical processes may also alter the 1D flux power spectrum, such as the effects of fluctuations in the ionizing background [38], patchy reionization [52], modification of the thermal history [53], and galactic outflows [54]. These additional factors are yet absent in many of the present cosmological simulations. To sum up, the uncertainties from both numerical and physical

factors prevent us from constraining the mass of FDM precisely, unless models and analyses with percent level precisions are available. A hydrodynamic simulation handling all of the uncertainties is needed in the future to set the correct constraint on the FDM mass.

V. CONCLUSION

In this paper, we have extended our FDM smoothed-particle hydrodynamics methodology to cosmological N-body simulation. Unlike previous works in literature, we have implemented not only the FDM initial condition but also the QP effect to our cosmological N-body simulations. The correct transformation of QP from physical to comoving coordinates has been derived in this work. With this new technique, we have performed four different simulations, **CDM**, **FIC**, **FDM**, and **F23**. We have shown the difference of overdensity between **FIC** and **FDM** simulations. We have found that some granular structures located at higher density regions can be produced by QP. Remarkably, we are able to probe halos with mass smaller than $2 \times 10^{13} h^{-1} M_{\odot}$ in cosmological simulations based on our methodology.

The matter power spectra from our four simulations tell us that the impact from QP is non-trivial, as shown by the difference between **FIC** and **FDM**. Comparing with **CDM** in the region with wavenumber $k < 10 h^{-1} \text{Mpc}$, the power spectrum suppression due to the effect of initial condition is less than 1% at redshift $z = 4.2$, but the QP effect can cause $< 5\%$ suppression in the same region. Hence, the impact from QP on the power spectrum is more significant than that from initial conditions at low redshifts. Moreover, the QP effect also depends on the redshift. At high redshifts $z \sim 10$ the effect of modified initial condition is more important than QP, but vice versa at low redshifts $z \sim 0$. Considering the DM mass around 10^{-23} eV, the matter power spectrum of the simulation **F23** shows a large deviation from that of **CDM** in the wavenumber $k \gtrsim 2 h^{-1} \text{Mpc}$ region.

Using the results of these four different simulations, we then further studied the flux power spectrum of Lyman-alpha forest. We obtain the 1D flux power spectrum by integrating the 3D matter power spectrum taken from our simulation result. There is still suppression on the flux power spectra of **FDM** and **F23** on small scales compared to that of **CDM**. However, the difference between **FIC** and **CDM** is small, which indicates that the suppression due to the transfer function of FDM is consumed by the non-linear evolution. To summarize, by comparing the flux power spectra of different simulations, we demonstrate that the QP causes non-trivial effect on small scales, which could be important in the study of Lyman-alpha forest.

Finally, we discussed the uncertainties in simulations and models. As an example, we did a rough estimation and found that the average gas temperature T_0 and FDM mass m_{χ} are degenerate since a smaller m_{χ} or a higher T_0 both suppress the 1D flux power spectrum. We found that the current constraint on the average temperature of the gas is not accurate enough to exclude FDM mass $m_{\chi} > 10^{-22}$ eV, which is summarized in Table. II and Fig. 8.

We conclude that the QP plays an important role in structure formation and affects

the prediction for Lyman-alpha forest significantly. A further comprehensive hydrodynamic simulation including the QP and a precise constraint on the gas temperature of Lyman-alpha forest are needed to solidly set a lower bound on the FDM particle mass.

Acknowledgment

We would like to acknowledge Eric Armengaud and Vid Iršič for discussion and Lachlan Lancaster for useful suggestions. We also would like to acknowledge Lam Hui and Tom Broadhurst for useful comments. This work is partially supported by a CUHK Discretionary Fund and by the MoST of Taiwan under the grant no.: 105-2112-M-007-028-MY3.

Appendix A: detail of the comoving transformation

We show the full transformation of the QP from physical to comoving coordinates. The Lagrangian can be expressed as

$$L = \frac{1}{2}M\mathbf{v}^2 - \frac{\hbar^2}{2m_\chi^2} \frac{M}{\bar{\rho}} (\nabla\sqrt{\rho})^2 - M\phi(\mathbf{r}), \quad (\text{A1})$$

where M , v , m_χ , ρ , $\bar{\rho}$ and ϕ are mass and velocity of simulation particles, mass of FDM, density in physical coordinate, average density in physical coordinate and gravitational potential, respectively. The first, second and the third terms in Eq. (A1) are the kinetic energy, the potential energy arising from the QP and the gravitational potential energy, respectively. We follow the basic transformations

$$\begin{aligned} \mathbf{r} &= a\mathbf{x}, & \mathbf{v} &= \dot{\mathbf{r}} = a\dot{\mathbf{x}} + \dot{a}\mathbf{x}, & \rho &= \rho_x/a^3, \\ \nabla_x &= a\nabla_r, & \Delta_x &= a^2\nabla_r \cdot \nabla_r = a^2\Delta_r, \end{aligned} \quad (\text{A2})$$

which incorporate the scale factor a to account for the expansion of the universe. Here r denotes the physical coordinates and x denotes the comoving coordinates.

After including the transformations, the Lagrangian Eq. (A1) becomes

$$L = \frac{1}{2}M(a\dot{\mathbf{x}} + \dot{a}\mathbf{x})^2 - \frac{1}{a^2}K_{\rho x} - M\phi(\mathbf{x}), \quad (\text{A3})$$

where we define

$$K_{\rho x} = \frac{\hbar^2}{2m_\chi^2} \frac{M}{\rho_x} (\nabla_x\sqrt{\rho_x})^2. \quad (\text{A4})$$

The transformation of the Poisson equation can be written as

$$\Delta_r\phi = 4\pi G(\rho - \rho_\Lambda) \rightarrow \Delta_x\phi = \frac{4\pi G}{a}(\rho_x - \rho_{\Lambda x}), \quad (\text{A5})$$

where ρ_Λ is the density of the cosmological constant. In order to simplify the equation, we perform a canonical transformation on the Lagrangian

$$\begin{aligned} L &= L - \frac{dF(\mathbf{x}, t)}{dt}, \\ F &= \frac{1}{2}Ma\dot{\mathbf{x}}^2, \end{aligned} \tag{A6}$$

which does not change the equation of motion. Now the Lagrangian can be written as

$$L = \frac{1}{2}Ma^2\dot{\mathbf{x}}^2 - \frac{1}{a^2}K_{\rho x} - M\Phi, \tag{A7}$$

where we define $\Phi = \phi + (1/2)a\ddot{\mathbf{x}}^2$ for simplicity. Consequently, the Poisson equation is converted to

$$\Delta_x \Phi = \Delta_x(\phi + \frac{1}{2}a\ddot{\mathbf{x}}^2) = \frac{4\pi G}{a}(\rho_x - \rho_{\Lambda x}) + 3a\ddot{\mathbf{x}}. \tag{A8}$$

From the second equation of the Friedmann equations,

$$\frac{\ddot{a}}{a} = -\frac{4\pi G}{3}(\bar{\rho} - \rho_\Lambda) = -\frac{4\pi G}{3a^3}(\bar{\rho}_x - \rho_{\Lambda x}), \tag{A9}$$

one can obtain

$$\Delta_x \Phi = \frac{4\pi G}{a}(\rho_x - \bar{\rho}_x). \tag{A10}$$

Additionally, we define $\Psi = a\Phi$ and acquire $\Delta_x \Psi = 4\pi G(\rho_x - \bar{\rho}_x)$. Now the Lagrangian can be written as

$$L = \frac{1}{2}Ma^2\dot{\mathbf{x}}^2 - \frac{1}{a^2}K_{\rho x} - \frac{1}{a}M\Psi. \tag{A11}$$

Hence we can define the canonical momentum as

$$\mathbf{p} = \frac{\partial L}{\partial \dot{\mathbf{x}}} = Ma^2\dot{\mathbf{x}}, \tag{A12}$$

and write down the Hamiltonian

$$H = \frac{1}{2Ma^2}\mathbf{p}^2 + \frac{1}{a^2}K_{\rho x} + \frac{1}{a}M\Psi. \tag{A13}$$

As a consequence, we obtain the equations of motion

$$\begin{aligned} \dot{\mathbf{x}} &= \frac{\partial H}{\partial \mathbf{p}} = \frac{\mathbf{p}}{Ma^2}, \\ \dot{\mathbf{p}} &= -\frac{\partial H}{\partial \mathbf{x}} = -\frac{1}{a^2}\nabla_x K_{\rho x} - \frac{M}{a}\nabla_x \Psi. \end{aligned} \tag{A14}$$

In the equations of motion, the terms for gravity and QP have prefactors $1/a$ and $1/a^2$ respectively, and hence we need to treat them separately in the comoving coordinates. In the physical coordinates, we can deal with these two terms simultaneously since $a = 1$.

Appendix B: simulation uncertainty

The systematic uncertainties in N-body simulation are well studied. The matter power spectrum is affected by the methodology of generating initial condition for simulations, such as the choice between the first order Lagrangian perturbation theory (1LPT) and the second order Lagrangian perturbation theory (2LPT) can introduces $\sim 6\%$ difference in the matter power spectrum, as reported in Ref. [31]. The halo mass function in the large mass end is sensitive at $\sim 7\%$ level to the choice of the finite simulation box size, which can be corrected owing to their clear nature [32].

The uncertainty resulting from different N-body simulation codes is numerically hard to estimate, and the origin of the discrepancies among different codes is also barely known. Such kind of issues are comprehensively discussed in Ref. [33]. Roughly speaking, the discrepancy between different codes is within 10% in the matter power spectrum and halo mass function. However, Ref. [34, 35] reported a 20% discrepancy in the center and 10% in the outskirts of the halo by comparing the halo density profile from several different codes.

Unlike the $\mathcal{O}(10\%)$ errors in the N-body simulations, the uncertainties involved in hydrodynamic simulations are much larger. Usually, a considerable uncertainty can be introduced due to the treatments of the gaseous component. As demonstrated in Ref. [34–37], a large inconsistency of the galaxy structure can be caused by using different hydrodynamic codes. Quantitatively, the errors of the gas density and temperature in the centers of the galaxies are about one to two orders of magnitude, estimated by comparing different hydrodynamic codes.

The one-dimension (1D) flux power spectrum of Lyman alpha forest can also contain some level of uncertainties, e.g., see the code comparison in Ref. [50, 51]. For hydrodynamic simulations using ENZO [55] and using Gadget2, there is also a $\sim 5\%$ difference in the 1D flux power spectrum and $\sim 10\%$ difference in the probability distribution of density and temperature. Moreover, for simulations using AREPO [56] and Gadget2, there are also 5% difference in their 1D flux power spectra.

-
- [1] N. A. Bahcall, L. M. Lubin, and V. Dorman, *The Astrophysical Journal Letters* **447**, L81 (1995), astro-ph/9506041.
 - [2] J. Einasto, A. Kaasik, and E. Saar, *Nature* **250**, 309 (1974).
 - [3] D. Clowe *et al.*, *The Astrophysical Journal Letters* **648**, L109 (2006), astro-ph/0608407.
 - [4] P. Ade *et al.*, *Astronomy & Astrophysics* **594**, A13 (2016), 1502.01589.
 - [5] M. Tegmark *et al.*, *The Astrophysical Journal* **606**, 702 (2004), astro-ph/0310725.
 - [6] D. H. Weinberg, J. S. Bullock, F. Governato, R. K. de Naray, and A. H. Peter, *Proceedings of the National Academy of Sciences* **112**, 12249 (2015), 1306.0913.
 - [7] A. Pontzen and F. Governato, *Nature* **506**, 171 (2014), 1402.1764.
 - [8] P. Colin, V. Avila-Reese, and O. Valenzuela, *The Astrophysical Journal* **542**, 622 (2000).

- [9] D. N. Spergel and P. J. Steinhardt, *Physical Review Letters* **84**, 3760 (2000), astro-ph/9909386.
- [10] W. Hu, R. Barkana, and A. Gruzinov, *Physical Review Letters* **85**, 1158 (2000), astro-ph/0003365.
- [11] D. J. Marsh, *Physics Reports* **643**, 1 (2016), 1510.07633.
- [12] X. Du, C. Behrens, and J. C. Niemeyer, *Monthly Notices of the Royal Astronomical Society* **465**, 941 (2017), 1608.02575.
- [13] P. Mocz *et al.*, (2017), 1705.05845.
- [14] J.-W. Lee, (2017), 1704.05057.
- [15] R. Hlozek, D. Grin, D. J. Marsh, and P. G. Ferreira, *Physical Review D* **91**, 103512 (2015), 1410.2896.
- [16] B. Bozek, D. J. Marsh, J. Silk, and R. F. Wyse, *Monthly Notices of the Royal Astronomical Society* **450**, 209 (2015), 1409.3544.
- [17] H.-Y. Schive, T. Chiueh, and T. Broadhurst, *Nature Physics* **10**, 496 (2014), 1406.6586.
- [18] V. Iršič, M. Viel, M. G. Haehnelt, J. S. Bolton, and G. D. Becker, *arXiv preprint arXiv:1703.04683* (2017).
- [19] E. Armengaud, N. Palanque-Delabrouille, C. Yèche, D. J. Marsh, and J. Baur, *arXiv preprint arXiv:1703.09126* (2017).
- [20] T. Kobayashi, R. Murgia, A. De Simone, V. Iršič, and M. Viel, *ArXiv e-prints* (2017), 1708.00015.
- [21] M. Rees *et al.*, *Monthly Notices of the Royal Astronomical Society* **218**, 25P (1986).
- [22] S. Ikeuchi, *Astrophysics and space science* **118**, 509 (1986).
- [23] D. H. Weinberg, R. Dav'e, N. Katz, and J. A. Kollmeier, *arXiv preprint astro-ph/0301186* (2003).
- [24] A. Arinyo-i Prats, J. Miralda-Escudé, M. Viel, and R. Cen, *Journal of Cosmology and Astroparticle Physics* **2015**, 017 (2015).
- [25] M. Viel, M. G. Haehnelt, and V. Springel, *Mon. Not. Roy. Astron. Soc.* **354**, 684 (2004), astro-ph/0404600.
- [26] N. Palanque-Delabrouille *et al.*, *Astron. Astrophys.* **559**, A85 (2013), 1306.5896.
- [27] S. López *et al.*, *Astron. Astrophys.* **594**, A91 (2016), 1607.08776.
- [28] P. Mocz and S. Succi, *Physical Review E* **91**, 053304 (2015), 1503.03869.
- [29] J. Veltmaat and J. C. Niemeyer, *arXiv preprint arXiv:1608.00802* (2016).
- [30] J. Zhang, Y.-L. S. Tsai, K. Cheung, and M.-C. Chu, *arXiv preprint arXiv:1611.00892* (2016).
- [31] B. LHuillier, C. Park, and J. Kim, *New Astronomy* **30**, 79 (2014).
- [32] J. Bagla and J. Prasad, *Monthly Notices of the Royal Astronomical Society* **370**, 993 (2006).
- [33] K. Heitmann, M. White, C. Wagner, S. Habib, and D. Higdon, *The Astrophysical Journal* **715**, 104 (2010).
- [34] J.-h. Kim *et al.*, *The Astrophysical Journal Supplement Series* **210**, 14 (2013).
- [35] F. Sembolini *et al.*, *Monthly Notices of the Royal Astronomical Society* **457**, 4063 (2016).
- [36] B. W. Oshea, K. Nagamine, V. Springel, L. Hernquist, and M. L. Norman, *The Astrophysical Journal Supplement Series* **160**, 1 (2005).
- [37] F. Vazza *et al.*, *Monthly Notices of the Royal Astronomical Society* **418**, 960 (2011).

- [38] L. Hui, J. P. Ostriker, S. Tremaine, and E. Witten, *Phys. Rev.* **D95**, 043541 (2017), 1610.08297.
- [39] H. Mo, F. Van den Bosch, and S. White, *Galaxy formation and evolution* (Cambridge University Press, 2010).
- [40] V. Springel, *Monthly Notices of the Royal Astronomical Society* **364**, 1105 (2005).
- [41] W. Hu, R. Barkana, and A. Gruzinov, *Phys. Rev. Lett.* **85**, 1158 (2000), astro-ph/0003365.
- [42] D. J. Eisenstein and W. Hu, *The Astrophysical Journal* **496**, 605 (1998), astro-ph/9709112.
- [43] H.-Y. Schive, T. Chiueh, T. Broadhurst, and K.-W. Huang, *Astrophys. J.* **818**, 89 (2016), 1508.04621.
- [44] M. Crocce, S. Pueblas, and R. Scoccimarro, *Astrophysics Source Code Library* **1**, 01005 (2012).
- [45] A. Lewis and A. Challinor, *Astrophysics Source Code Library* (2011).
- [46] M. Viel, G. D. Becker, J. S. Bolton, and M. G. Haehnelt, *Physical Review D* **88**, 043502 (2013).
- [47] A. Rorai *et al.*, *Science* **356**, 418 (2017).
- [48] V. Iršič *et al.*, *Mon. Not. Roy. Astron. Soc.* **466**, 4332 (2017), 1702.01761.
- [49] S. R. Knollmann and A. Knebe, *Astrophys. J. Suppl.* **182**, 608 (2009), 0904.3662.
- [50] J. A. Regan, M. G. Haehnelt, and M. Viel, *Monthly Notices of the Royal Astronomical Society* **374**, 196 (2007).
- [51] S. Bird *et al.*, *Monthly Notices of the Royal Astronomical Society* , sts590 (2013).
- [52] R. Cen, P. McDonald, H. Trac, and A. Loeb, *Astrophys. J.* **706**, L164 (2009), 0907.0735.
- [53] A. Garzilli, A. Boyarsky, and O. Ruchayskiy, (2015), 1510.07006.
- [54] M. Viel, J. Schaye, and C. M. Booth, *Mon. Not. Roy. Astron. Soc.* **429**, 1734 (2013), 1207.6567.
- [55] G. L. Bryan *et al.*, *The Astrophysical Journal Supplement Series* **211**, 19 (2014).
- [56] V. Springel, *Proceedings of the International Astronomical Union* **6**, 203 (2010).